TÜBİTAK

Turkish Journal of Physics

http://journals.tubitak.gov.tr/physics/

Research Article

Turk J Phys
(2015) 39: 280 – 287

doi:10.3906/fiz-1407-2

Nanocrystalline NiO structure: preferred oriented growth

Ali RAHMATI[1,2,*], **Soheila MARDANI**[1,3]
[1]Department of Physics, Faculty of Science, Vali-e-Asr University of Rafsanjan, Rafsanjan, Iran
[2]Nanostructure Laboratory, Faculty of Science, Vali-e-Asr University of Rafsanjan, Rafsanjan, Iran
[3]Faculty of Physics, University of Isfahan, Isfahan, Iran

Received: 03.07.2014 • **Accepted/Published Online:** 06.02.2015 • **Printed:** 30.11.2015

Abstract: Nickel oxide (NiO) nanostructures were deposited on Si (100), potassium bromide (KBr), and glass slide substrates at room temperature by the evaporation technique. The prepared samples were annealed at temperatures of 400 °C and 600 °C in air atmosphere. The structure, morphology, crystalline phase, optical properties, and chemical bonding of nanocrystalline nickel oxide were investigated by scanning electron microscopy (SEM), X-ray diffraction (XRD), UV-visible absorption spectrum, and FT-IR spectroscopy.

XRD results and SEM images showed that nickel oxide nanoparticles have preferred orientation with uniform size distribution. The as-deposited films showed preferred orientation (texture) growth. As the films were annealed, the crystallites were agglomerated to form bigger particles. Optical properties were identified by measuring transmittance using a UV-Vis spectrophotometer. Optical constants such as the refractive index n, the extinction coefficient k, and the films' thickness and roughness were calculated from transmittance data using a reverse engineering method. As the sample annealed, the ad-atom surface mobility increased, and smaller crystallites agglomerated to form bigger ones.

Key words: NiO nanocrystallite, preferred orientation growth, thermal evaporation

PACS: 81.15.Fg, *43.35.Ns, 68.60.Bs, 78.20.-e

1. Introduction

Nickel oxide (NiO) nanostructures have various applications in electrochromic display devices, antiferromagnetic layers, and solar thermal absorbers, and as cathode material for alkaline batteries [1–4]. Some other interesting electronic properties of NiO nanostructures are their wide band gap range of 3.6–4.0 eV [5] and their p-type conductivity, which make them favorable materials for electronic device applications [6,7]. Nanostructures of NiO can be deposited by various chemical and physical methods such as the chemical bath deposition/solution growth technique, reactive sputtering, and the vacuum evaporation technique [8–11].

In the present work, a single cubic phase of NiO nanostructures with a nearly uniform particle size was deposited by the evaporation method. The properties of the NiO nanostructures were characterized by Vis/near IR transmission, X-ray diffraction, FT-IR spectra, and scanning electron microscopy (SEM).

2. Experiments and methods

Nanostructures of NiO were deposited by the thermal evaporation technique from nickel oxide powder (purity of 99.999%) at a background pressure of 5×10^{-4} mbar and room temperature. The evaporated species were

*Correspondence: a.rahmati@vru.ac.ir

condensed onto ultrasonically precleaned Si (100), potassium bromide (KBr), and glass slide substrates to study chemical bonding and structural and optical properties. The prepared samples were annealed at temperatures of 400 °C and 600 °C.

Optical studies were performed by measuring transmittance in the wavelength region of 350–800 nm using a spectrophotometer (Cary-100, UV-Visible) at room temperature. Optical constants of nanostructures such as the refractive index $n(\lambda)$, the extinction coefficient $k(\lambda)$, and the film thickness were calculated using spectral fitting or reverse engineering.

Structural characterization was done ex situ by an X-ray diffractometer (XRD, D8 Advance Bruker) with a CuKα radiation source in a 2θ scan mode. The lattice constant was extracted from the peak position of the XRD reflection. Fourier transform infrared (FTIR) spectra were recorded in the transmission mode in the range of 400–4000 cm^{-1} by using an FTIR spectrophotometer. Film morphology was determined using a coupled scanning electron microscope (SEM, Philips XL30).

3. Results and discussion

3.1. Optical properties

The optical properties of nanostructures have been investigated by various analytical and numerical methods [5–8]. For the calculation of optical constants of nanostructures such as the refractive index $n(\lambda)$, the extinction coefficient $k(\lambda)$, and the film thickness, transmittance data can be used. In this study, the transmittance data and the methods described below in the frame of the point-wise unconstrained minimization approach (PUMA) were utilized for the optical characterization of the as-deposited and annealed NiO film.

Figure 1 depicts normal (perpendicular) transmittance of the NiO film deposited on the glass slide by thermal evaporation. There is an easy approach for determination of optical constants, which depends on a single transmittance measurement. The refractive index n, the extinction coefficient k, and the thickness d of the polycrystalline NiO nanostructures studied here were determined from transmittance data by only using the PUMA approach and the code described by Birgin et al. [12]. This method implements the complex optical equations shown below, derived and formulated by Heavens [13] and Swanepoel [14]. The transmittance T of a

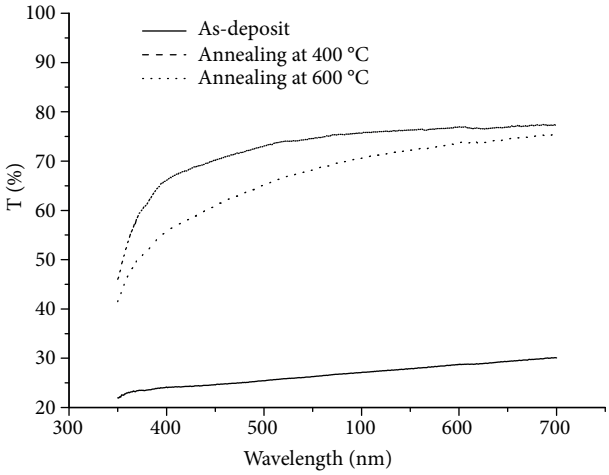

Figure 1. Transmission spectra of the as-deposited and annealed samples.

thin absorbing film deposited on a thick transparent substrate is given by:

$$T = T(\lambda, s(\lambda), d, n(\lambda), k(\lambda)) = \frac{A'x}{B' - C'x + D'x^2} \tag{1}$$

where

$$A' = 16s(n^2+k^2), B' = [(n+1)^2+k^2][(n+1)(n+s^2)+k^2]$$

$$C' = \left[\left(n^2-1+k^2\right)\left(n^2-s^2+k^2\right) - 2k^2\left(s^2+1\right)\right]2\cos\phi - k\left[2\left(n^2-s^2+k^2\right) + \left(s^2+1\right)\left(n^2-1+k^2\right)\right]2\sin\phi$$

$$D' = \left[(n-1)^2+k^2\right]\left[(n-1)\left(n-s^2\right)+k^2\right], \phi = \frac{4\pi nd}{\lambda}, x = \exp(-\alpha d), \alpha = \frac{4\pi k}{\lambda}$$

where s is the refractive index of the substrate, n and k are respectively the real and imaginary parts of the refractive index of the film, d is the film thickness, λ is the wavelength of the incident light, and α is the absorption coefficient of the film. Birgin et al. [12] showed that the continuous least square solution of the estimation problem is the solution (d, n, and k) of:

$$\text{Minimize} \int_{\lambda_{\min}}^{\lambda_{\max}} |T(\lambda, s(\lambda), d, n(\lambda), k(\lambda)) - T^{meas}(\lambda)|^2 d\lambda \tag{2}$$

subject to some physical constraints.

The glass slide substrate was too thick and the addition of interference effects resulting from multiple reflections in the substrate was eliminated. The experimental transmittance data were compared with theoretical values (Eq. (1)), according to PUMA [12]. The difference between the two values was minimized (Eq. (2)) until a best solution was achieved for the refractive index n, the extinction coefficient k, and the film thickness d. Poelman et al. [15] reviewed and tested the PUMA approach, showing that it produces excellent estimates of optical constants of nanostructures.

Figure 1 shows the transmittance spectra of the deposited films on the glass slide substrate. Figures 2 and 3 show the dispersions of the calculated refractive index n and extinction coefficient k, respectively, as functions of wavelengths in the 300–1100 nm range. The refractive index n is shown to decrease as the wavelength of the incident photon increases; however, at higher wavelengths of the incident photon, the refractive index tends to remain constant. For the samples annealed at temperatures of 400 °C and 600 °C, the values of the refractive index are lower than those of the as-deposited ones, due to an increase in porosity in the NiO structure. The absorption coefficient of the NiO films is related to the extinction coefficient through $\alpha = 4\pi k/\lambda$ (Figure 4).

To determine the film thickness, d, several thicknesses are extracted from the fitting process (Eq. (2)) and then the mean of d is calculated. The maximal deviation from the mean value of the thickness can be considered as a well estimation of the film's roughness. The film thickness and its roughness are given in the Table.

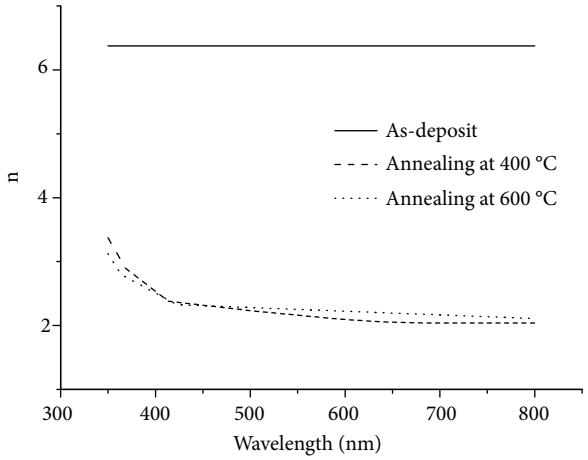

Figure 2. Dispersion of the refractive index (n) of the as-deposited and annealed samples.

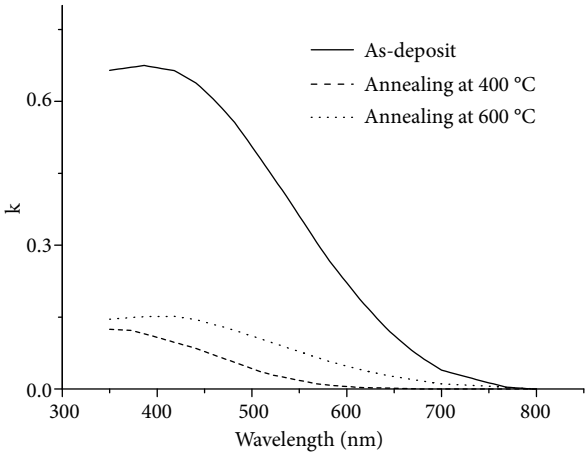

Figure 3. Dispersion of the extinction coefficient (k) of the as-deposited and annealed samples.

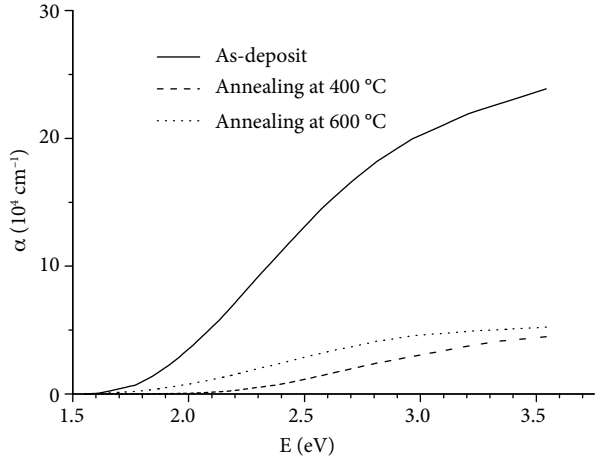

Figure 4. Absorption coefficient of the as-deposited and annealed samples.

Table. Films' thickness (d) and roughness of the as-deposited and annealed NiO thin films.

Sample	d (nm)	Roughness (nm)
As-deposited	84	2.3
Annealed at 400 °C	83	2.7
Annealed at 600 °C	73	3.8

3.2. Structural properties

Figure 5 depicts the XRD pattern of the as-deposited and annealed NiO nanostructures. The XRD analysis, when compared with JCPDS (File No 40–1191), reveals the formation of very well preferred orientated nickel oxide with a (220) direction. The lattice constant of the cubic NiO structure is calculated as 8.76 Å, which is found to be expanded with respect to the JCPDS value. As a result, the annealed NiO nanostructures get enough time to diffuse to an energetically favorable site. This could also arise due to an excess of sufficient energy needed by an atom to move to a proper site in forming a bigger crystallite.

3.3. Chemical bonding with FT-IR

The formation of nickel oxide on a KBr substrate was also identified by FT-IR spectral studies (Figure 6) at the different annealing temperatures, and its infrared absorption was deduced. Weak peaks were found between 445 and 490 cm^{-1} assigned to the Ni-O stretching [16].

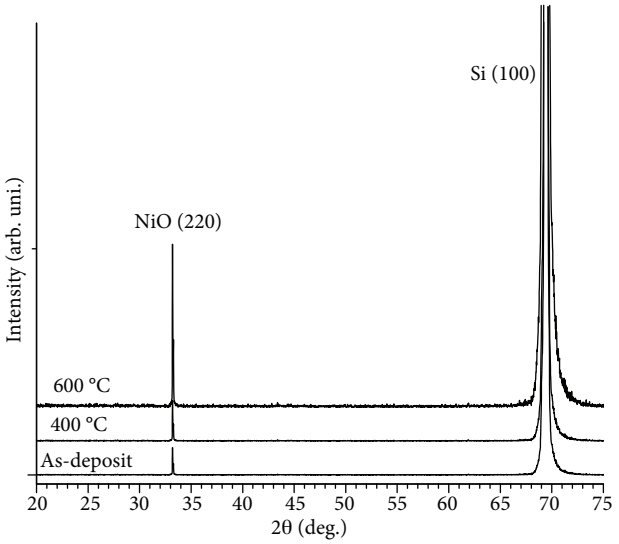

Figure 5. XRD pattern of the as-deposited and annealed nickel oxide nanostructures at temperatures of 400 °C and 600 °C.

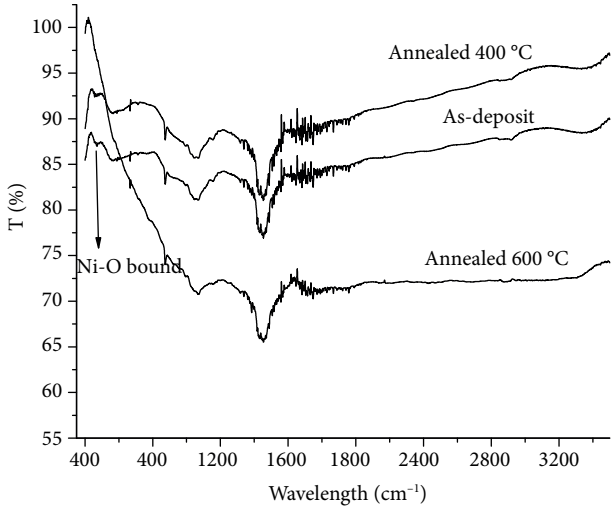

Figure 6. FT-IR spectra of the as-deposited and annealed nickel oxide nanostructures at temperatures of 400 °C and 600 °C.

3.4. Morphological properties

The SEM images of the samples are shown in Figure 7. The SEM picture reveals that the particles are more or less spherical in shape. Moreover, the particle size distribution is nearly uniform. As the samples annealed, the surface mobility of the ad-particles increased and consequently the smaller crystallites agglomerated to form bigger ones.

3.5. Estimating the temperature of resistance heaters

In the design of electrical heaters for evaporation systems, the temperature of heated furnaces plays an important role in the deposition process [16]. Under a simplifying assumption it is possible to draw connections between the electrical power (P) supplied and the furnace temperature reached. By noting that P is simply given by i^2R, where i and R are the current and resistance, respectively, for a metallic furnace [17]:

$$P = i^2R = i^2R(0)\left[\frac{T}{T(0)}\right]^n \tag{3}$$

This equation assumes that the electrical resistance, R(T), of metals can be approximated over a broad high temperature (T) range by the relation $R(T) = R(0)[T/T(0)]^n$, where R(0) is the value at reference temperature T(0) (i.e. room temperature, RT), and n is a constant generally close to 1. In tungsten, n is selected to be 1.20 [17]. Under deposition conditions, $R(0) = 0.0029e$ and $i = 150A$. A complementary approach may be used,

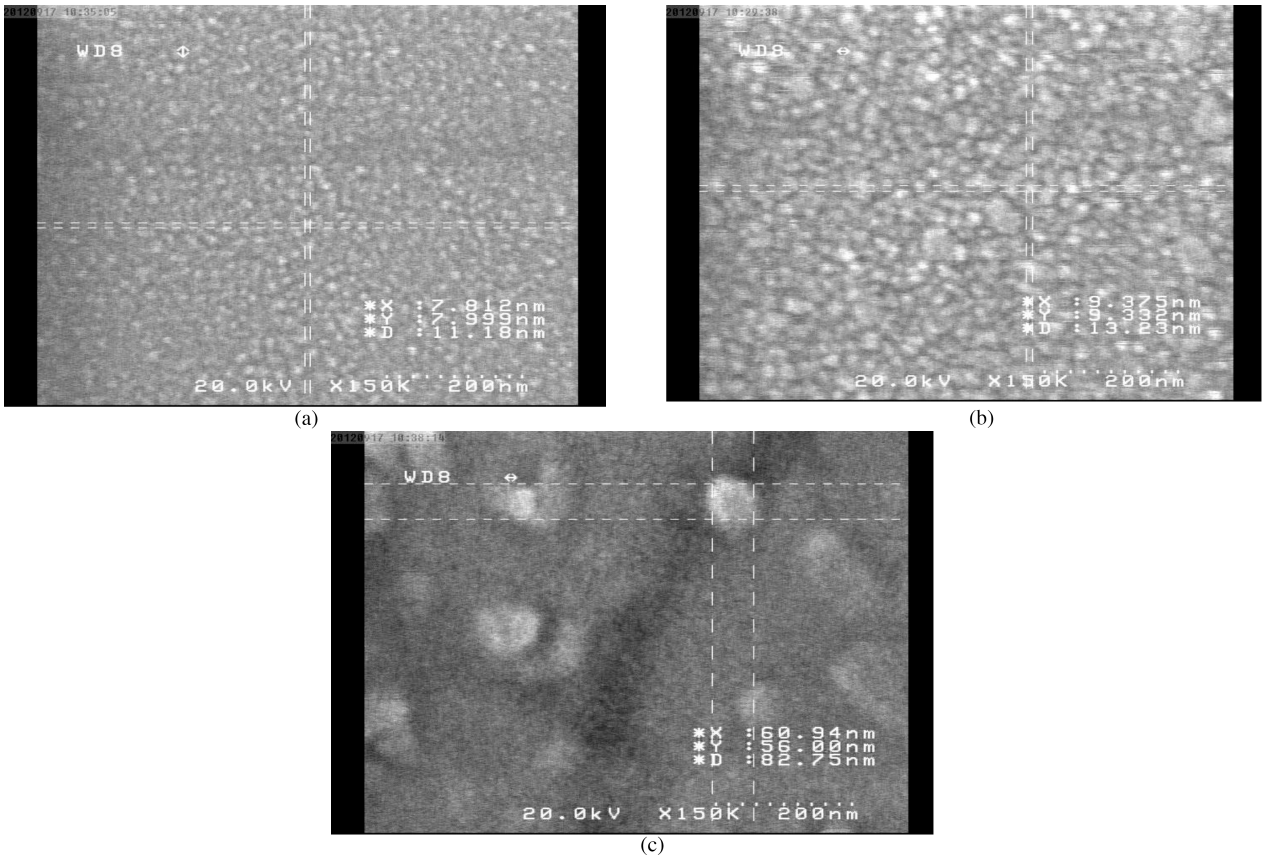

Figure 7. The SEM images of the as-deposited (a) and annealed nickel oxide nanostructures at temperatures of 400 °C (b) and 600 °C (c).

assuming that all of the input electrical power dissipated is thermally radiated from the furnace surface. In this case the Stefan–Boltzmann law yields the defining equation for the radiated power (P_r) [17]:

$$P_r = \varepsilon \sigma A_s (T^4 - T(0)^4 \tag{4}$$

where ε is the emissivity, σ is Stefan's constant ($\sigma = 5.67 \times 10^{-8} w/m^2 - k^4$), and A_s is the furnace surface area ($A_s = 2\text{them}^2$). The ε for the tungsten plate is 0.04 [18]. The tungsten furnace is considered to be rectangular to eliminate the effect of complex geometries. The temperature of the resistance heaters was estimated to be 1180.5 K.

3.6. Evaporation rate and vapor pressure of the materials

According to Hertz, Knudsen, and Langmuir's experiments, the evaporation rate condensed from both liquid and solid surfaces [17] is:

$$\Phi_e = \frac{\alpha_e N_A (P_e - P_h)}{(2\pi MRT)^{1/2}} \tag{5}$$

where Φ_e is the evaporation flux in a number of atoms (or molecules) per unit area, per unit time, and P_e and P_h are the equilibrium vapor pressure at temperature and the hydrostatic pressure acting on the evaporant,

respectively. α_e is the coefficient of evaporation, which has a value between 0 and 1. When $\alpha_e = 1$ and P_h is zero, the maximum evaporation rate is realized. An expression for the maximum value of Φ_e is [17]:

$$\Phi_e = \left(\frac{3.513 \times 10^{22}}{(MT)^{\frac{1}{2}}} \right) P_e(molecules/cm^2 - s) \tag{6}$$

where P_e is expressed in torr. A useful variant of this formula is

$$\Gamma_e = 5.84 \times 10^{-2} \left(\frac{M}{T} \right)^{1/2} P_e \left(\frac{g}{cm^2 - s} \right) \tag{7}$$

where Γ_e is the mass evaporation rate.

The connection between temperature and vapor pressure is the Clausius–Clapeyron equation, which for condensed phases (both liquid and solid) vapor equilibria can be written as [17] :

$$\frac{dP}{dT} = \frac{\Delta H(T)}{T \Delta V} \tag{8}$$

The changes in enthalpy, ΔH(T), and volume, ΔV, refer to differences between the vapor (v) and the particular condensed phase (c) from which it originates, while T is the transformation temperature in question. Since $\Delta V = V_v - V_c$, and normally the volume of vapor considerably exceeds that of the condensed solid or liquid phase, $\Delta V \approx V_v$. If the gas is assumed to be perfect, V_v = RT/P, and Eq. (11) may be rewritten as [17]:

$$\frac{dP}{dT} = \frac{P \Delta H(T)}{RT^2} \tag{9}$$

Hence,

$$lnP_{(torr)} = \int \frac{\Delta H(T)}{RT^2} dT \tag{10}$$

The enthalpy ΔH and heat capacity C_p of each species were calculated using the following relation [19]:

$$\Delta H = \Delta H_{298} + \int_{298}^{T} C_P dT \tag{11a}$$

$$C_p = a + b \times 10^{-3} T + c \times 10^6 T^{-2} + d \times 10^{-6} T^2 \tag{11b}$$

where

$$\Delta H_{298} = 309.5 kj.mol^{-1}, a = 39.82, b = 1.54 \times 10^{-3}, C = -0.57 \times 10^6 \text{ and } d = 0 for NiO.$$

The vapor pressure and the evaporation flux of NiO were calculated to be 6×10^{-44} torr and 1.14399×10^{-14} molecules/cm^2-s under the given deposition conditions, respectively.

4. Conclusion

NiO films were deposited on Si (100), potassium bromide (KBr), and glass slide substrates at room temperature by the thermal evaporation technique. The prepared samples were annealed at temperatures of 400 °C and 600 °C in an air atmosphere. The chemical bonding and the structural, optical, and morphological properties of the annealed samples were compared with those of the as-deposited films.

Nickel oxide nanocrystallites have well preferred orientation with a uniform size distribution. As the films were annealed, the crystallites agglomerated to form bigger particles. The optical constants such as the refractive index n, the extinction coefficient k, and the films' thickness and roughness were calculated from transmittance data. As the samples annealed, the surface mobility of ad-atoms increased, which induced the smaller crystallites to agglomerate and form bigger grains.

Acknowledgment

This work was funded by Vali-e-Asr University of Rafsanjan, Rafsanjan, Iran.

References

[1] Bögner, M.; Fuchs, A.; Scharnagl, K.; Winter, R.; Doll, T.; Eisele, I. *Sens. Actuators B. Chem.* **1998**, *47*, 145–152.

[2] Yoshimura, K.; Miki, T.; Tanemura, S. *Jpn. J. Appl. Phys.* **1995**, *34*, 2440–2446.

[3] Fujii, E.; Tomozawa, A.; Torii, H.; Takayama, R. *Jpn. J. Appl. Phys.* **1996**, *35*, 328–330 .

[4] Li, Q. Y.; Wang, R. N.; Nie, Z. R.; Wang, Z. H.; Wei, Q. *J. Colloid Interf. Sci.* **2008**, *320*, 254–258.

[5] Sato, H.; Minami, T.; Takata, S.; Yamada, T. *Thin Solid Films* **1993**, *236*, 27–31.

[6] Ajuba, A. E.; Ezeugwu, S. C.; Asogwa, P. U.; Ezema, F. I. *Chalcogenide Letters* **2010**, *10*, 573–579.

[7] Krishnakumar, S. R.; Liberati, M.; Grazioli, C.; Veronese, M.; Turchini, S.; Luches, P.; Valeri, S.; Carbone, C. *J. Magn. Magn. Mater.* **2007**, *310*, 8–12.

[8] Sartale, S. D.; Lokhande, C. D. *Material Chemistry and Physics* **2001**, *72*, 100–104.

[9] Anuar, K.; Zukarnian, Z.; Sauravanan, N.; Zuriyatina, A; Sharing, R. *Material Science (Medziagotyra)* **2004**, *10*, 157–161.

[10] Chion, J. W.; Talaga, D. S.; Zink, J. I. *B. Mater. Sci.* **1997**, *27*, 1208–1212.

[11] Oriaku C. I.; Cosuwa, J. *Journal of Ovonic Research* **2009**, *5*, 213–218.

[12] Birgin, E. G.; Chambouleyron, I.; Martinez, J. M. *J. Comput. Phys.* **1999**, *151*, 862–880.

[13] Heavens, O. S. *Optical Properties of Nano-structures*; Dover: New York, NY, USA, 1991.

[14] Swanepoel, R. *J. Phys. E Sci. Instrum.* **1983**, *16*, 1214–1222.

[15] Poelman, D.; Smet, P. F. J. *Phys. D Appl. Phys.* **2003**, *36*, 1850–1857.

[16] Dharmaraj, N.; Prabu, P.; Nagarajan, S.; Kim, C. H.; Park, J. H.; Kim, H. Y. *Mater Sci. Eng. B* **2006**, *128*, 111–114.

[17] Ohring, M. *Materials Science of Nano-structures, Deposition & Structure,* 2nd ed.;, Academic Press: New York, NY, USA, 2002.

[18] Lassner, E.; Schubert, W. D. *Tungsten: Properties, Chemistry, Technology of the Elements, Alloys, and Chemical Compounds;* Kluwer Academic, Plenum Publisher: New York, NY, USA, 1999.

[19] Binnewies, M.; Milke, E. *Thermochemical Data of Elements and Compounds*, 2nd ed.; Wiley-VCH: Berlin, Germany, 2002.